Gaussian pre-filtering for uncertainty minimization in digital image correlation using numerically-designed speckle patterns

Paolo Mazzoleni [a,b,c], Fabio Matta [b,*], Emanuele Zappa [c], Michael A. Sutton [d], Alfredo Cigada [c]

[a] Rolls-Royce plc, MV-GF, Victory Road, P.O. Box 31, Derby DE24 8BJ, UK
[b] Dept. of Civil and Environmental Engineering, University of South Carolina, 300 Main Street, Columbia, SC 29208, USA
[c] Dept. of Mechanical Engineering, Politecnico di Milano, via La Masa 1, 20156 Milan, Italy
[d] Dept. of Mechanical Engineering, University of South Carolina, 300 Main Street, 29208 Columbia, SC, USA

Received 18 April 2014
Received in revised form 21 July 2014
Accepted 4 August 2014
Available online 16 September 2014

1. Introduction

The design and implementation of effective speckle patterns on two-dimensional measurement surfaces are key to enhance the accuracy of digital image correlation (DIC), along with suitable displacement and strain field estimation algorithms [1,2]. The accuracy of DIC measurements was studied as a function of mean speckle size and subset size, for which desirable ranges were reported [3–5]. Several techniques have been used to create speckle patterns, depending on the specimen dimensions and materials. Spray paint or toner powders are typically used for larger specimens, whereas lithography is preferred for smaller patterns [6]. The resulting speckle patterns are characterized by non-repetitiveness and high contrast between light and dark areas. As shown by Wang et al. [7] for translation in two planar directions, x and y, the form of the covariance matrix for the displacement vector, $\mathbf{d}$, is written in Eq. (1):

$$\mathrm{Var}(\mathbf{d}) \cong \sigma_I^2 \begin{bmatrix} \sum_{\text{subset}} \left(\frac{\partial I}{\partial x}\right)^2 & \sum_{\text{subset}} \left(\frac{\partial I}{\partial x}\frac{\partial I}{\partial y}\right) \\ \sum_{\text{subset}} \left(\frac{\partial I}{\partial y}\frac{\partial I}{\partial x}\right) & \sum_{\text{subset}} \left(\frac{\partial I}{\partial y}\right)^2 \end{bmatrix}^{-1} \quad (1)$$

* Corresponding author. Tel.: +1 803 777 1917; fax: +1 803 777 0670. *E-mail addresses:* paolomazzoleni@yahoo.it (P. Mazzoleni), fmatta@sc.edu (F. Matta), emanuele.zappa@polimi.it (E. Zappa), sutton@sc.edu (M.A. Sutton), alfredo.cigada@polimi.it (A. Cigada).

where: **d** is the displacement vector, (u,v), in the x and y direction, respectively; σ_I is the standard deviation in the intensity pattern noise (gray levels); and $I=I(x,y)$ is the reconstructed deformed intensity pattern (gray levels). If the gradients in both directions are independent, then the off-diagonal term tends to zero, and the matrix is approximately diagonal. In this case, the standard deviation in each displacement component, σ_u and σ_v, can be written per Eq. (2):

$$\mathrm{Var}(u) \cong \frac{\sigma_I^2}{\sum_{\text{subset}} \left(\frac{\partial I}{\partial x}\right)^2} \Rightarrow \sigma_u \cong \frac{\sigma_I}{\sqrt{\sum_{\text{subset}} \left(\frac{\partial I}{\partial x}\right)^2}}$$

$$\mathrm{Var}(v) \cong \frac{\sigma_I^2}{\sum_{\text{subset}} \left(\frac{\partial I}{\partial y}\right)^2} \Rightarrow \sigma_v \cong \frac{\sigma_I}{\sqrt{\sum_{\text{subset}} \left(\frac{\partial I}{\partial y}\right)^2}} \quad (2)$$

where "high contrast" corresponds to the summation of high gradients in intensity within a subset, increasing the denominator and reducing variability in the measured displacement. With maximum range between brightest and darkest regions, smooth transitions in intensity across the camera's dynamic range can be accurately reconstructed by interpolation algorithms, offering the potential for high accuracy when performing subset matching with DIC algorithms. Thus, the gray level distribution within the speckle pattern can be used as a measure of the effectiveness of a speckle pattern [8]. Schreier et al. [9] proposed the implementa-tion of low-pass image filters in the pre-processing stage to produce blurring, either by defocusing the camera's optics prior to image acquisition or by applying digital filters on the acquired image data. The latter option is more attractive as it allows for better control of the parameters selected to produce blurring. In fact, digital filters are commonly used in image processing. For example, Berg et al. [10] and Cantatore et al. [11] implemented digital filters to produce image blurring, thereby improving the accuracy of algorithms for edge detection.

The effect of digital image pre-filtering on the uncertainty in two-dimensional DIC measurements is discussed in this paper for the specific case of high-contrast speckle patterns whose particle shape, mean size and on-center spacing are designed for use in efficient patterning of large areas ("designer patterns"). This case represents instances where numerically-designed speckle patterns are applied to the measurement surface through different techniques, such as using laser-printed adhesive coatings on fiber-reinforced polymer composite coupons [12], or spray-painting through a flexible polymer stencil placed against the surface of concrete and masonry specimens [13] as demonstrated in Fig. 1. These solutions are especially appealing and practical for large regions of interest (i.e., having sides of the order of meters) on full-scale specimens such as structural concrete and masonry walls (Fig. 12) or portions of bridge girders, when spray-painting or using toner powders is less practical and may pose aliasing problems whereas using relatively large speckles (e.g., through time-consuming manual painting) may result in an insufficient spatial resolution [13]. The resulting "designer patterns" are characterized by speckles with well-defined edges and consistent shape and spacing, making their frequency content fundamentally different from that of typical spray-painted patterns. In the latter case, pre-processing image blurring can be effective in reducing the bias error [9,14]. However, the concurrent reduction in noise level and intensity pattern gradients (i.e., numerator and denominator for σ_u and σ_v in Eq. (2), respectively) may result in a negligible change or even an increase in measurement uncertainty.

The methodology followed in this study employs numerical simulations where images are pre-processed using Gaussian low-pass (blurring) filters [15]. First, the effect of blurring is examined on a numerically built speckle pattern as a function of the standard deviation of the Gaussian kernel (i.e., filter cut-off frequency). The resulting patterns are used to quantify the DIC measurement uncertainty for the case of constant, linear, quadratic and cubic displacement fields and the associated strain fields. The robustness of the simulation procedure is verified through experiments where a planar specimen with a "designer pattern" is subjected to a constant displacement. For comparison purposes, the effect of image blurring is also assessed on a speckle pattern that is representative of typical spray-painted ones [16,17] subjected to constant displacements. Finally, the stability of the relation between Gaussian standard deviation and measurement uncertainty is tested via numerical simulations using different levels of

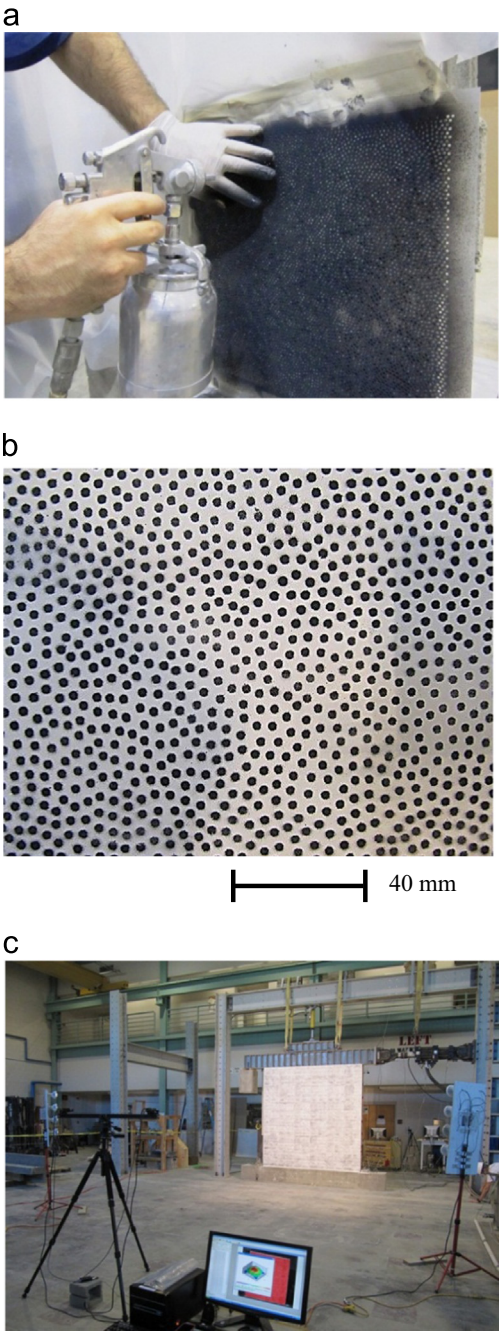

Fig. 1. Numerically designed speckle pattern on 2.43×2.49 m concrete and masonry wall surface: (a) spray painting through stencil; (b) close-up of 150×120 mm speckle pattern area; and (c) stereo vision system setup with specimen ready for in-plane load test [13].

image noise representative of real-case scenarios, subset sizes, and frequency contents in the "designer pattern".

2. Methodology

The effect of pre-processing image blurring on DIC measurement uncertainty is investigated via numerical simulations on a predefined speckle pattern, as recently demonstrated by Zappa et al. [18] for the case of dynamic applications. The methodology is summarized in the flow chart in Fig. 2. The simulations are implemented using Matlab Image Processing Toolbox (The MathWorks, Inc., Natick, MA). A 4000 $\times$ 4000 pixel array with eight-bit quantization is numerically constructed and an ordinate grid of black circular speckles is superimposed as shown in Fig. 3(a). The speckles have a diameter of 45 pixel and on-center spacing of 60 pixel along the horizontal, x, and vertical, y, directions. Then, each of the orthogonal coordinates, x and y, of the centroid of each speckle is perturbed by adding an integer displacement, thus avoiding image resampling. The integer value is randomly extracted from a uniform distribution in the $\pm$25-pixel range to render the high-resolution speckle pattern in Fig. 3(b).

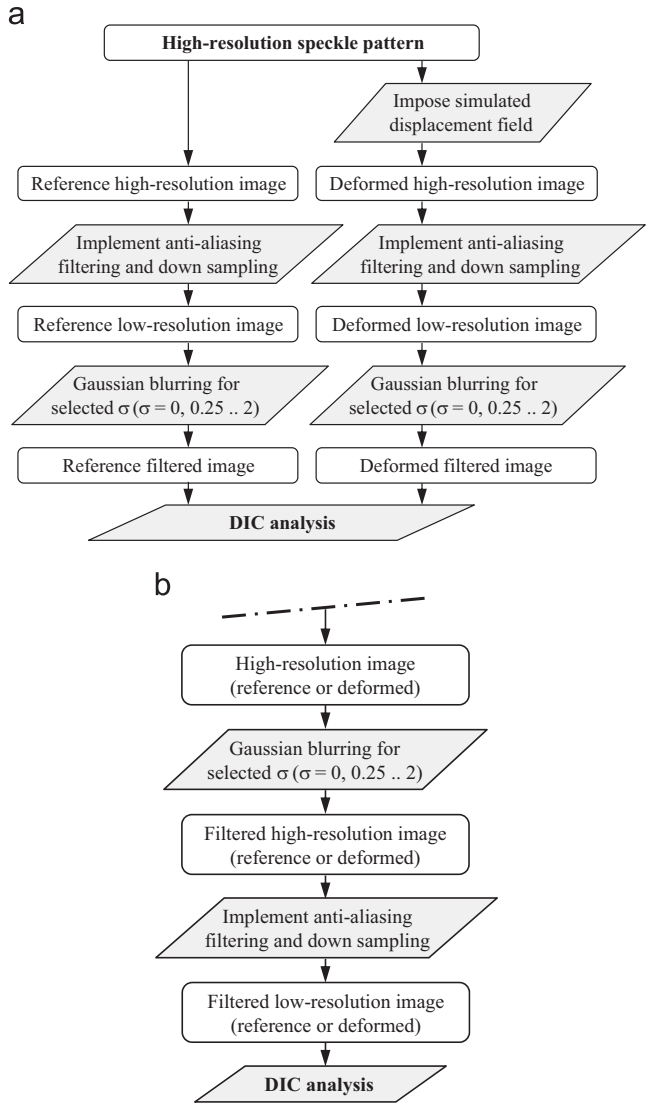

Fig. 2. Flowchart of methodology: (a) Gaussian blurring of down-sampled ("low-resolution") image; and (b) modified subroutine for Gaussian blurring of high-resolution pattern prior to down-sampling.

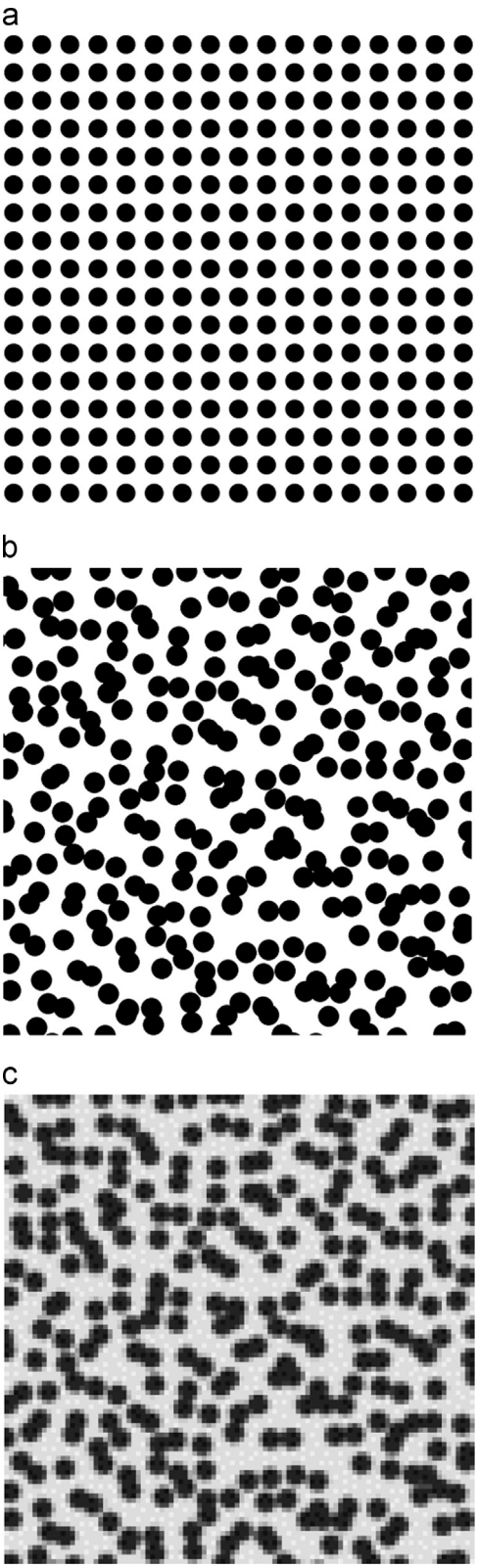

Fig. 3. Numerical simulation of speckle pattern: (a) high-resolution ordinate grid, 1000 $\times$ 1000 pixel subset; (b) high-resolution speckle pattern, 1000 $\times$ 1000 pixel subset; and (c) low-resolution speckle pattern, 100 $\times$ 100 pixel subset.

The intensity pixel range in the resulting image is then narrowed from 0 to 255 (identifying speckles and background, respectively) to 30–225, thus following a routine practice to prevent pixel saturation in real-case scenarios. Fig. 3(c) shows a 100 $\times$ 100 pixel

subset of the resulting 400 × 400 pixel low-resolution speckle pattern, which is produced by anti-aliasing filtering and down-sampling by ten times the original high-resolution speckle pattern in Fig. 3(b). A window-based finite impulse response (FIR) low-pass filter is used for the anti-aliasing filtering of the high-resolution images before down-sampling, where the cut-off frequency is a function of the scaling factor. This operation aims at removing frequency content that could be aliased in the low-resolution images [17]. Quantization noise is introduced by the eight-bit image representation. In the low-resolution speckle pattern, the speckles have a diameter of 4.5 pixel and an average on-center spacing of 6 pixel. The resulting coverage factor (i.e., percentage of dark pixels in the image) is 42%, which lies within the desirable 40–70% range to minimize measurement uncertainty [19].

The derivation of low-resolution images by down-sampling their high-resolution counterparts is pursuant to mimicking real-case scenarios. A similar approach, where numerical binning was implemented in lieu of low-pass anti-aliasing filtering, was enlisted by Reu [17] to quantify the errors in DIC when simulating a rigid target shift (i.e., zero strain). Any deformations may be imposed on a given high-resolution image, which simulates an actual DIC measurement area, while the associated down-sampled low-resolution image simulates the image acquired using a digital camera. This procedure does not require arbitrary interpolation of the final image, which would be necessary when simulating sub-pixel displacements and deformations directly in the final image. In this study, pre-defined displacement and strain fields are imposed on the high-resolution speckle pattern. For the case of simulated rigid motion (constant displacement), the imposed integer displacements in the high-resolution images result in sub-pixel displacements in the low-resolution images [17]. Con-versely, when a variable displacement field is imposed in order to simulate strains, then bicubic image re-sampling of the high-resolution images is implemented [20]. The effect of Gaussian filtering of the reference and deformed low-resolution images is studied through a parametric analysis of the standard deviation of the Gaussian kernel vis-à-vis DIC measurement uncertainty. In particular, filtering is applied to: (a) down-sampled images following the methodology in Fig. 2(a) and (b) high-resolution images prior to down-sampling to assess the effect of the order of the blurring operation following the methodology in Fig. 2(b).

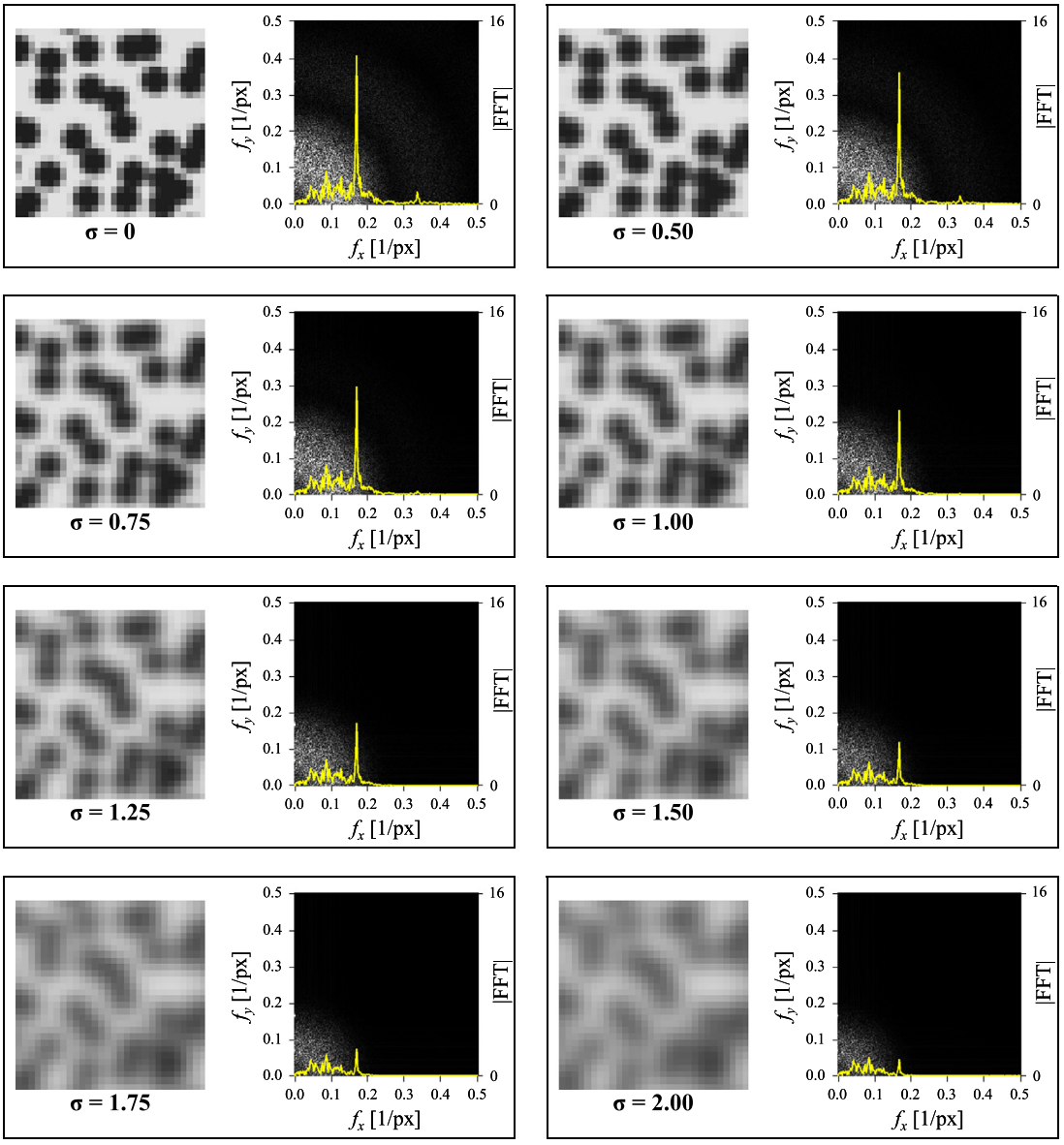

Fig. 4. Blurring effect of Gaussian filter on low-resolution speckle pattern (30 × 30 pixel subset) for different standard deviations, σ, and associated image spectra.

Gaussian filters are two-dimensional filters [15] that are often used for image processing purposes. The impulse response of Gaussian filters is the well-known bell-shaped function whose smoothness enables the minimization of ringing, while binomial filtering enables the definition of computationally efficient Gaus-sian filters for Weierstrass transform [21]. In the (x,y) spatial domain, the convolution matrix of Gaussian filters is rendered as a zero-mean Gaussian function described by Eq. (3):

$$G(x,y)=\frac{1}{2\pi\sigma^2}e^{-\left(\frac{x^2+y^2}{2\sigma^2}\right)} \tag{3}$$

where σ denotes the standard deviation of the Gaussian "bell". In the frequency domain, different standard deviations of the Gaus-sian kernel describe a family of filters with different cut-off frequencies.

The Gaussian standard deviation, σ, used in this parametric study ranges from 0 to 2 pixel when applied to down-sampled images (Fig. 2(a)), and from 0 to 20 pixel when applied to the original ($10\times$) high-resolution images (Fig. 2(b)). A zero σ indi-cates the absence of filters, and increasing values are associated with filters that produce more blurring. For a given σ, the filter is applied to the image matrices through their convolution with the Gaussian kernel. The effect of blurring of down-sampled images is illustrated in Fig. 4 for 30×30 pixel portions of the reference 400×400 pixel images. The image spectral amplitudes are shown together with the superimposed |FFT| amplitude profile along the x direction, and the mean value of the spectra is set to zero to facilitate graphical representation; similar trends are obtained when blurring and then down-sampling the high resolution images. In Fig. 4, the peak amplitude is associated with a frequency that corresponds to the average spacing of the speckles. It is noted that the main frequency content lies in the f_x range below the main peak, and the effect of moderate blurring ($\sigma\leq 1$ pixel) is to minimize the high-frequency contributions to the right of the peak while slightly reducing the amplitude of the low-frequency content. The magnitude of the frequency response function, |FRF|, for different Gaussian standard deviations is shown in Fig. 5; by filtering using $\sigma\leq 1$ pixel, it is shown that the higher frequencies are reduced without noticeable perturbations in the main range, whereas further increases in blurring results in the progressive attenuation of the main frequency content.

The DIC analysis of the filtered images is performed using the software Vic-2D 2009 (Correlated Solutions, Inc., Columbia, SC). A 15×15 pixel subset size and step of 5 pixel are considered. The subset size was selected to provide a nominally isotropic and homogeneous random pattern. An eight-tap optimized interpolation method is implemented. A zero-normalized sum of squared difference correlation criterion is selected to compensate for the scaling and offset in the intensity pattern, thus mimicking real-case applications. A 5×5 subset decay kernel matrix is used to derive strain values [6].

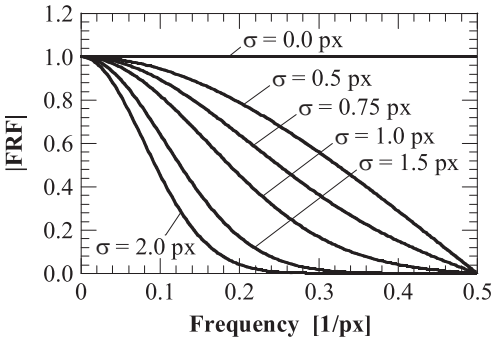

Fig. 5. Magnitude of frequency response function of Gaussian filters.

3. Effect of image filter pre-processing

The results for the following cases are presented and discussed separately: (a) constant horizontal (along x) displacement and zero strain; and (b) higher-order (linear, quadratic and cubic) displacement functions with non-zero horizontal strain fields (zero vertical strain is imposed). In particular, the simulation of cubic displacement fields aims at testing the filters when the subset matching cannot be exact, since the DIC software used implements a second-order matching shape function [6].

3.1. Constant displacement

3.1.1. Gaussian filtering of down-sampled images

The reference high-resolution image is subjected to a constant horizontal displacement from 0 to 10 pixel in 1 pixel steps, thereby obtaining 11 images. The derived low-resolution (400×400 pixel) images having a displacement range from 0 to 1 pixel in 0.1 pixel steps are then filtered. The effect of image filtering on the bias error of DIC measurements is illustrated in Fig. 6(a). Here, the mean difference (error) between the displacement measured using Vic-2D 2009, $u_{\mathrm{DIC},ij}$, and the numerically imposed displace-ment, $u_{\mathrm{IMP},ij}$, is presented as a function of the imposed displace-ment for representative values of the Gaussian standard deviation, σ, and is computed per Eq. (4)

$$E_u=\frac{\sum_{i=1}^{N_R}\sum_{j=1}^{N_C}(u_{\mathrm{DIC},ij}-u_{\mathrm{IMP},ij})}{N_R N_C} \tag{4}$$

where N_R and N_C indicate the number of rows and columns of the displacement matrix, respectively, and $u_{\mathrm{IMP},ij}$ is constant for any i and j as a constant displacement is imposed to the entire image. When the images are unfiltered ($\sigma=0$ pixel), the typical trend of the interpolation bias is noted where the error function E_u has a sinusoidal shape in the sub-pixel displacement range, and reduces to zero at half pixel and at integer pixel values [7]. The maximum bias error is reduced by more than half when a filter with a standard deviation σ of 0.5 pixel is applied. Further increases in σ result in the progressive reduction in bias to near-zero values throughout the entire sub-pixel displacement range, thus indicat-ing that filtering enables the minimization of the average sub-pixel interpolation bias for pure translation cases. It is emphasized that zero E_u indicates only that the measured displacement values are distributed randomly around those of the imposed displacements (without a systematic bias on the measurement mean).

Fig. 6(b) presents the data dispersion (i.e., measurement uncertainty without bias contribution), which is given by the standard deviation of the measured displacements, STDE_u, as a function of the imposed displacement for representative values of σ. STDE_u is computed per Eq. (5):.

$$\mathrm{STDE}_u=\sqrt{\frac{\sum_{i=1}^{N_R}\sum_{j=1}^{N_C}(u_{\mathrm{DIC},ij}-\overline{u}_{\mathrm{DIC}})^2}{N_R N_C}} \tag{5}$$

where $\overline{u}_{\mathrm{DIC}}$ is the average measured displacement. It is noted that image blurring produces a minimization of the data dispersion for Gaussian standard deviations in the range 0.5–1 pixel.

The maximum amplitude of the bias error is strongly dependent on the test conditions, especially image noise and speckle pattern [17], and is difficult to estimate. In addition, in actual physical tests, the data variability is typically much larger than the bias effect, whose trend becomes evident only when averaging the displacements measured on multiple subsets subjected to the same displacement. As a result, the bias error on the displace-ment measured on a single subset cannot be precisely quantified

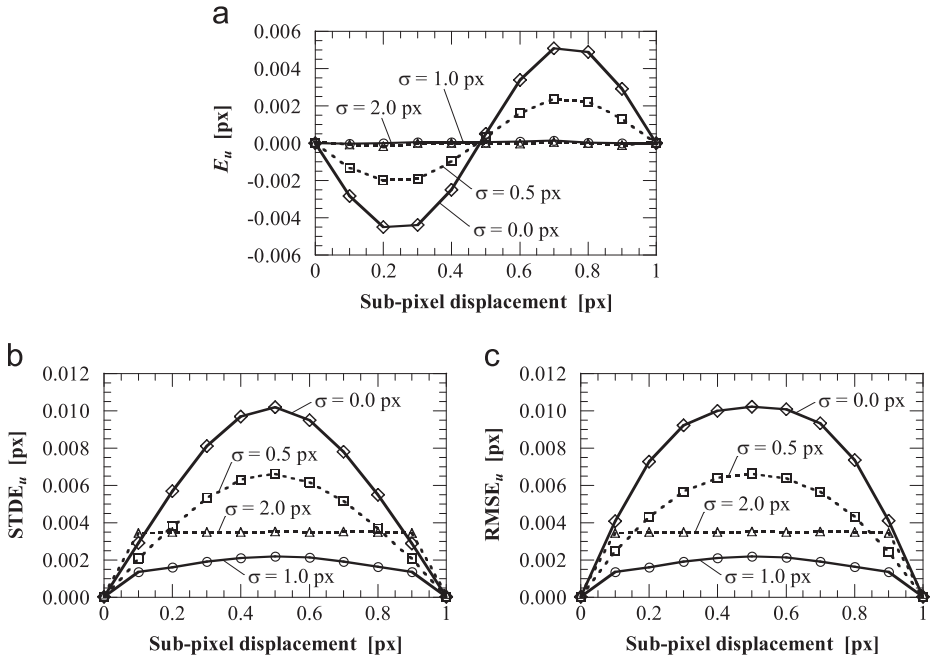

Fig. 6. Effect of Gaussian blurring ($0 \le \sigma \le 2$ pixel) of down-sampled images on measurement bias, standard deviation, and uncertainty for constant displacement: (a) E_u, (b) STDE$_u$, and (c) RMSE$_u$ as function of imposed sub-pixel displacement.

(and thus compensated for) and contributes to the measurement uncertainty. Therefore, the effect of image filtering on the DIC measurement uncertainty, where the contribution of both of bias and variability are included, is determined based on the root mean squared error, RMSE$_u$, which is computed per Eq. (6)

$$\mathrm{RMSE}_u = \sqrt{\frac{\sum_{i=1}^{N_R}\sum_{j=1}^{N_C}(u_{\mathrm{DIC},ij} - u_{\mathrm{IMP},ij})^2}{N_R N_C}} = \sqrt{{E_u}^2 + {\mathrm{STDE}_u}^2} \tag{6}$$

The measurement uncertainty of a calibrated (i.e., with no bias) transducer is defined as the standard deviation of repeated measurement data [22]. For the purpose of this study, the effect of bias is incorporated in Eq. (6), where the squared difference between measured and imposed values is used in lieu of that between mean and measured values.

The effect of image filtering on the uncertainty of DIC measurements is illustrated in Fig. 6(c), where RMSE$_u$ is presented as a function of the imposed displacement for representative values of σ. The zero RMSE$_u$ value in correspondence with integer pixel values (0, 1) of the imposed displacement reflects the fact that no noise is introduced in the simulated images. A similar trend is noted for σ=0, 0.5 and 1 pixel, where the uncertainty is symmetrically distributed in a quasi-parabolic fashion with respect to its maximum value at a displacement of 0.5 pixel, and decreases at increasing levels of blurring. For larger values of σ (up to 2 pixel), the maximum uncertainty increases and remains nearly constant in the entire sub-pixel range. Therefore, for the case of constant displacements, the DIC measurement uncertainty is minimized when applying a Gaussian pre-processing image filter with a standard deviation (and associated cut-off frequency) near 1 pixel, whereas a higher uncertainty is attained with less or more blurring filters. This finding is illustrated in Fig. 7(a), where the mean RMSE$_u$ for each RMSE$_u$ curve for a given value of the Gaussian standard deviation, σ, is plotted as a function of the associated σ to conveniently show the relation between measure-ment uncertainty and image blurring. Through the application of a blurring filter with σ=1 pixel, the mean RMSE$_u$ is reduced by 77% with respect to that of the unfiltered set of images (σ=0 pixel). Similar results are obtained for standard deviations in the indicative range 0.75–1.25 pixel, with a higher rate of increase in uncertainty for values below 0.75 pixel and above 1.25 pixel. Therefore, the effect of image blurring on the intensity pattern noise and image gradients (i.e., the numerator and denominator in Eq. (2), respectively) is such that the measurement uncertainty is minimized for σ in the range 0.75–1.25 pixel when using down-sampled images with the speckle pattern in Fig. 3(b) and (c).

The relation between measurement uncertainty and σ is illustrated in Fig. 7(b), where the mean root mean squared error, RMSE$_\varepsilon$, for each curve of horizontal strain measured for a given σ is plotted as a function of the associated σ, with RMSE$_\varepsilon$ for a given displacement being computed per Eq. (7)

$$\mathrm{RMSE}_\varepsilon = \sqrt{\frac{\sum_{i=1}^{N_R}\sum_{j=1}^{N_C}(\varepsilon_{\mathrm{DIC},ij} - \varepsilon_{\mathrm{IMP},ij})^2}{N_R N_C}} \tag{7}$$

where the notation is similar to that of Eq. (6) and $\varepsilon_{\mathrm{IMP},ij}$=0 for any i and j when a zero strain is imposed to the entire image. The trend of mean RMSE$_\varepsilon$ in Fig. 7(b) is similar to that of the mean RMSE$_u$ in Fig. 7(a), which is expected since the strain values, $\varepsilon(x)$, are given as partial derivatives of the associated displacement functions, $\partial u(x)/\partial x$.

3.1.2. Gaussian filtering of high-resolution images before down-sampling

Following the procedure in Fig. 2(b), Gaussian filtering was applied on the high-resolution images prior to down-sampling to assess the effect of the order of the blurring operation in comparison to Figs. 6 and 7. The bias error, E_u, data dispersion as the standard deviation of the measured displacements, STDE$_u$, and measurement uncertainty as the root mean squared standard error (RMSE$_u$) for translations between 0 and 1 pixel are presented for $0 \le \sigma \le 2$ pixel in Fig. 8. In Fig. 9, the relation between measurement uncertainty and image blurring is illustrated by plotting the mean RMSE$_u$ for each RMSE$_u$ curve for a given value of the Gaussian standard deviation, σ, as a function of the associated σ.

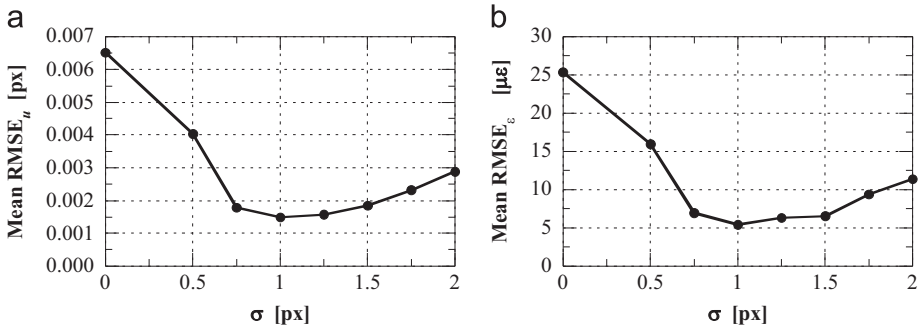

Fig. 7. Relation between measurement uncertainty and Gaussian blurring of down-sampled images for constant displacement: (a) mean value of RMSE$_u$ and (b) mean value of RMSE$_\varepsilon$ for $0 \le \sigma \le 2$ pixel.

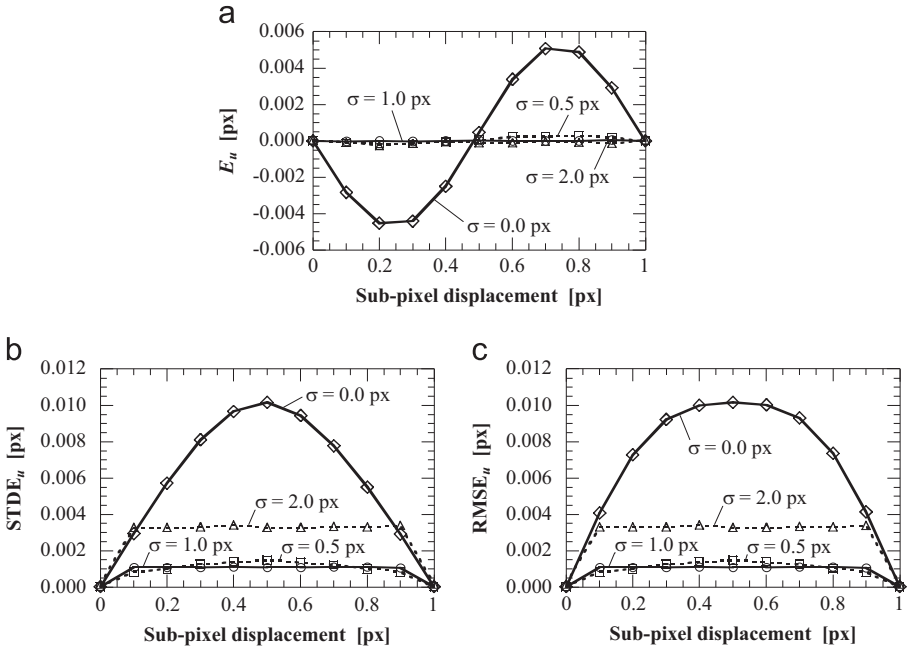

Fig. 8. Effect of Gaussian blurring ($0 \le \sigma \le 2$ pixel) of high-resolution images (followed by down-sampling) on measurement bias, standard deviation, and uncertainty for constant displacement: (a) E_u, (b) STDE$_u$, and (c) RMSE$_u$ as function of imposed sub-pixel displacement.

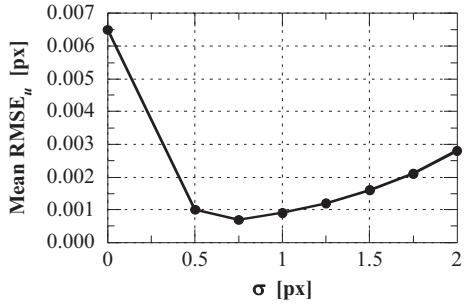

Fig. 9. Relation between measurement uncertainty and Gaussian blurring of high-resolution images (followed by down-sampling) for constant displacement: mean value of RMSE$_u$ for $0 \le \sigma \le 2$ pixel.

As shown in Fig. 6(a) and Fig. 8(a), the correct bias error form is recovered when no blurring occurs. However, when blurring the high-resolution image, a negligible bias is obtained for all σ values, which is an improvement with respect to the application of Gaussian filters on the down-sampled images. Comparison of Fig. 6(b) with Fig. 8(b) and of Fig. 6(c) with Fig. 8(c) indicate that the results are similar in both cases, with the main difference being a nearly uniform error metric from 0.1 to 0.9 pixel of translation when applying the Gaussian filter to the high-resolution images.

The comparison of Fig. 7(a) with Fig. 9 shows similar trends in the mean RMSE$_u$, with the main difference being a lower minimum error at a lower Gaussian filter size (0.00074 for σ=0.75 pixel as opposed to 0.0015 for σ=1 pixel) when applying the Gaussian filter to the high-resolution images.

3.2. Experimental verification of simulation procedure

Experiments for the case of constant displacement fields were performed to verify the robustness of the simulation procedure. The speckle pattern in Fig. 3(b) was printed and affixed onto the smooth surface of a rigid plate. The plate was attached to a coordinate measuring machine (CMM). The 160 × 160 mm pattern was framed by the 400 × 400 pixel sub-area of a digital camera with resolution of 640 × 480 pixel (Prosilica GE680, Allied Vision Technologies GmbH, Stadtroda, Germany) and lens with a nominal focal length of 8 mm. The distance between the image plane and the speckle pattern was tuned to yield a conversion factor of approximately 2.5 pixel/mm. The actual value was estimated via camera calibration. Constant horizontal displacements from 0 to 1 pixel were imposed with 0.1 pixel steps, with a CMM displacement uncertainty of 2 μm (i.e., 0.005 pixel). The images acquired were pre-filtered using different σ values, and then analyzed using a 15 × 15 pixel subset size and step of 5 pixel.

It is noted that the position of the camera was assessed using a pose-estimation algorithm [23] to verify that the optical axis was perpendicular to the object surface, thus ensuring uniformity of the resultant displacement fields. To this end, a row of regularly spaced dark blobs was printed in known positions along the margin of the patterned area. By analyzing the position of the blobs in the acquired images, the relative three-dimensional position and orientation of the camera was estimated accurately and in real time, and the latter was corrected as needed. Possible effects of radial distortion of the lens were not compensated. In fact, the maximum imposed displacement of 1 pixel was reasonably expected to result in a negligible apparent strain. In addition, compensation of lens distor-tion effects entails a local approximation and resampling of the images, which may result in a loss of high-order brightness components that are of interest when studying Gaussian blurring. A mid-frequency discrete cosine transform (MF-DCT) algorithm [24] was used to verify and maximize the camera focus during the preparation of the experimental setup.

The effect of image filtering on the discrepancy between DIC measurements is illustrated in Fig. 10(a), where the mean discrepancy, D_u, between the measured displacement and that imposed by the CMM is presented as a function of the latter for representative values of σ. The mean discrepancy is computed similar to E_u per Eq. (4), where the CMM displacements are used in lieu of the numerically imposed displacements. The results are in reasonable agreement with those from the numerical simulations in Fig. 6(a) both in terms of sub-pixel (sinusoidal) trend and decrease in bias error at increasing σ. The inevitably larger absolute values, and in particular the irregular trends for CMM displacements ranging between 0.7 and 1 pixel, are reasonably attributed to variable accidental vibrations of the camera and its unisolated support, along with the uncertainty of the movements imposed through the CMM.

The effect of image filtering on the standard deviation discrepancy of the measured displacement, $STDD_u$, is illustrated in Fig. 10(b), where $STDD_u$ is presented as a function of the CMM displacement for representative values of σ. It is noted that image blurring minimizes the random component of the discrepancy ($STDD_u$) for Gaussian standard deviations in the range 0.5–1 pixel when using the "designer pattern" in Fig. 3(b) and (c), consistent with the results of the numerical simulation in Fig. 6(b).

Finally, the measurement uncertainty is evaluated based on the root mean squared displacement discrepancy, $RMSD_u$, which is computed by combining in quadrature D_u and $STDD_u$ (similar to Eq. (6) for $RMSE_u$, E_u and $STDE_u$). $RMSD_u$ is presented in Fig. 10(c) as a function of the displacement for representative

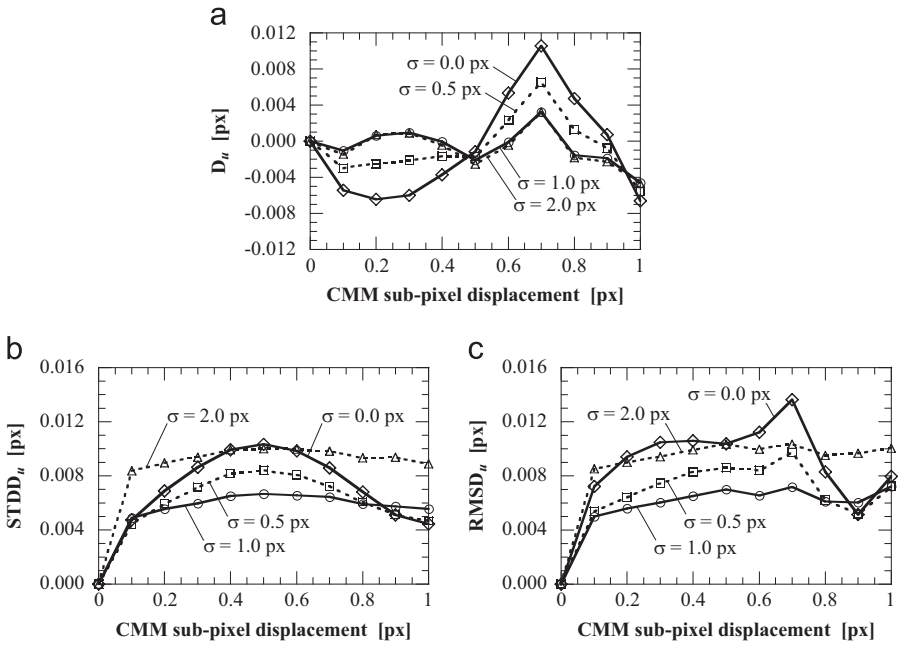

Fig. 10. Experimental verification of simulation procedure based on measurement discrepancy, standard deviation, and uncertainty: (a) D_u, (b) $STDE_u$, and (c) $RMSE_u$ as function of constant CMM sub-pixel displacement.

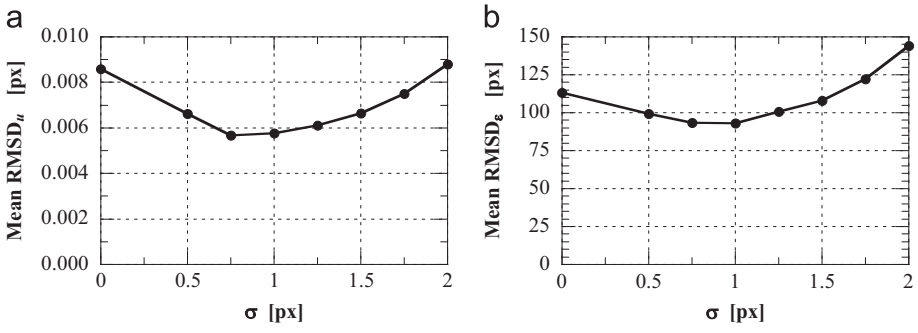

Fig. 11. Relation between measurement uncertainty and Gaussian blurring of down-sampled images for constant CMM displacement: (a) mean $RMSD_u$, and (b) mean $RMSD_\varepsilon$ for $0 \le \sigma \le 2$ pixel.

values of σ. The uncertainty is zero at zero CMM displacement as the reference image is compared with itself. For non-zero displacements, the uncertainty is minimized by applying a filter with standard deviation near 1 pixel, consistent with the simulation results in Fig. 6(b). It is important to note that both the bias error and random component of the measured displacements can be reduced through image blurring, contributing to the minimization of measurement uncertainty when using "designer patterns" as in Fig. 3(b) and (c). The experimental verification is concluded by assessing the mean $RMSD_u$ and mean root mean squared strain discrepancy, $RMSD_\varepsilon$, vis-à-vis the Gaussian standard deviation, σ, as illustrated in Fig. 11(a) and (b), respectively. The $RMSD_\varepsilon$ values are computed similar to $RMSE_\varepsilon$ per Eq. (7), where the CMM strains are used in lieu of the imposed strains. Measurement uncertainty is minimized using Gaussian filters with σ in the range 0.75–1.25 pixel, and increases with lower or higher levels of blurring. The results show a similar trend compared with the numerical simulations in Fig. 7(a) and (b), where the reduced effectiveness of filtering can be reasonably attributed to experimental factors such as vibrations and slight blurring induced by the optical elements.

3.3. Case of speckle pattern without well-defined particles

For comparison purposes, the effect of image blurring is assessed herein for a speckle pattern without well-defined particles, thus resulting in frequency spectra characterized by near-zero peaks, under constant displacements. The image set "High Contrast —Subpixel Shift in X and Y Experimental Images" with the speckle pattern shown in Fig. 12 was selected from the open-access "Digital Image Correlation Challenge" dataset [16]. This speckle pattern is representative of typical spray-painted ones and is fundamentally different from the "designer patterns" in Fig. 1 (b) and Fig. 3(b) and (c), whose frequency contents include more well-defined regions of non-zero content with non-zero peaks (Fig. 4). The image set was obtained by Reu [17] and includes images with shifts ranging from 0 to 1 pixel in 0.1 pixel steps.

The blurring effect is illustrated in Fig. 13 for a 30 × 30 pixel subset, where the image spectral amplitudes are shown together with the superimposed |FFT| amplitude profile along the x direction, and the mean value of the spectra is set to zero. It is noted that no appreciable changes in the non-zero frequency range and frequency peak are produced for σ up to 1 pixel. Conversely, for the representative "designer pattern" in Fig. 3(b) and (c), filtering with σ in the range 0.75–1 pixel results in images with similar contrast to that of the unfiltered "Digital Image Correlation Challenge" images as noted by comparing Fig. 4 with Fig. 13, but with a narrower non-zero frequency range and well-defined speckles as indicated by the reduced spectral peak at a spatial frequency $f_x \sim 1/6$ pixel^{-1}, clearly indicating a 6 pixel mean particle spacing (Fig. 4). As a result, limited blurring of well-defined edges produces images that maintain a good contrast and can be

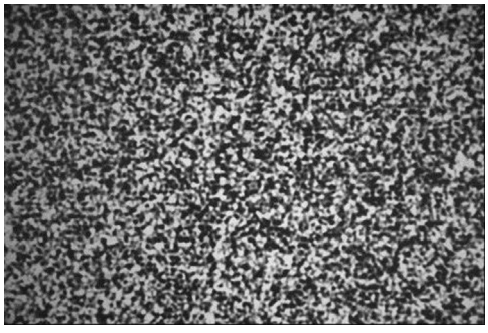

Fig. 12. Sample image of surface with speckle pattern without well-defined particle size [16,17].

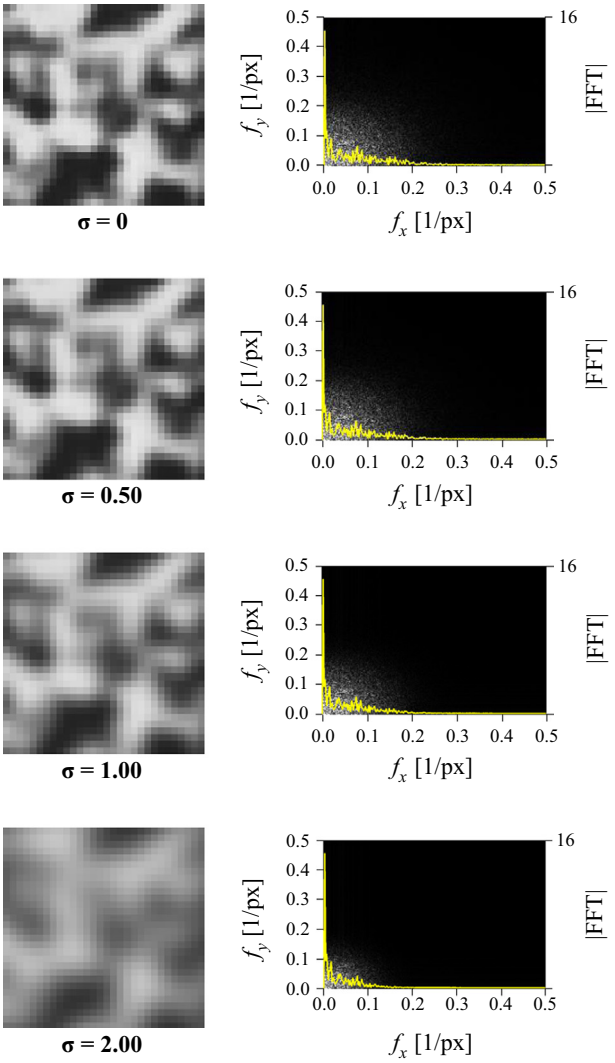

Fig. 13. Blurring effect of Gaussian filter on DIC Challenge speckle pattern (30 × 30 pixel subset) [16,17] for different standard deviations, σ, and associated image spectra.

matched more accurately, as demonstrated via numerical simulations (Figs. 6 and Fig. 8) and verified experimentally (Fig. 10).

For the speckle pattern without well-defined particles shown in Fig. 12 [16,17], the effect of image blurring on bias, standard deviation, and uncertainty for constant-displacement DIC measurements are illustrated in Fig. 14(a), Fig. 14(b) and (c), respectively. A moderate Gaussian filtering (σ=0.75–1 pixel) produces a decrease in bias error, consistent with the findings of Schreier et al. [8] and more recently Pan [14]. However, the effect on the intensity pattern noise level and gradients (Eq. (2)) is such that both standard deviation error and measurement uncertainty increase, albeit marginally. As noted by Wang [7], the measure-ment bias in DIC displacement data is composed of two parts:(a) noise-induced bias, which is a multiplicative combina-tion of interpolation inaccuracy and intensity pattern noise; and (b) interpolation induced bias. As shown in Fig. 14(a), when no blurring is present the well-known sinusoidal variation observed by Schreier et al. [9] and Pan [14] is noted. This trend is consistent with cases where the noise-induced bias is relatively small and the interpolation bias term is dominant. When blurring is present, there is a clear reduction in bias and a virtual elimina-tion of the sinusoidal trend, with a minimum occurring for σ in the range 0.75–1 pixel. Such a reduction can be qualitatively

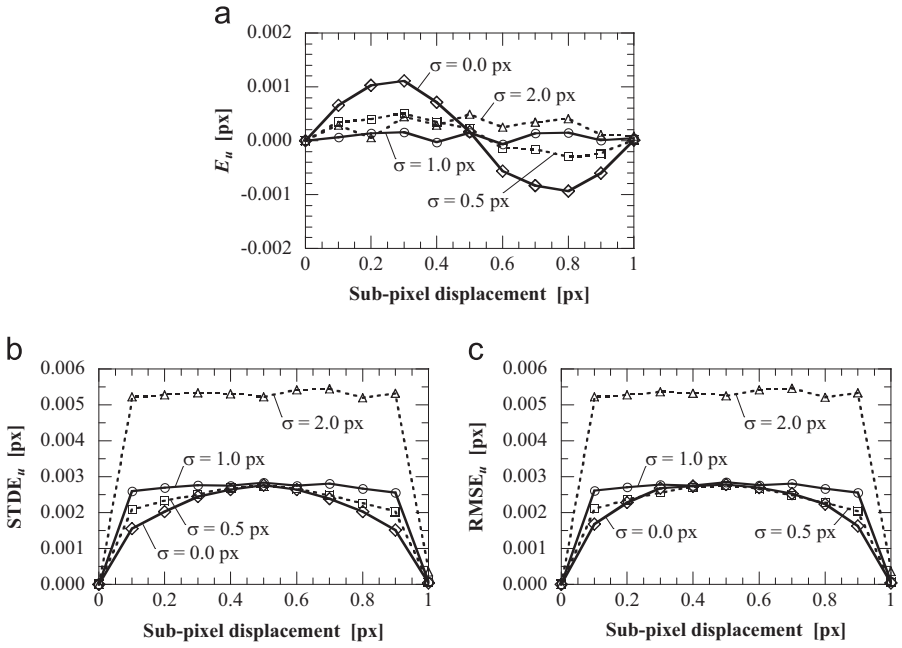

Fig. 14. Effect of Gaussian blurring ($0 \le \sigma \le 2$ pixel) on measurement bias, standard deviation, and uncertainty for constant displacement, for speckle pattern without well-defined particle size [16,17]: (a) E_u, (b) STDE$_u$, and (c) RMSE$_u$ as function of imposed sub-pixel displacement.

understood by the fact that the Gaussian filters smooth intensity transitions so that interpolation is more accurate in representing the intensity variations between pixels. A more detailed discussion is presented in Section 4 of this paper. Finally, it is noted that such trends should be qualitatively similar for both "designer patterns" and spray-painted patterns having similar spatial variability in speckle size, a fact that is confirmed by directly comparing Fig. 8 (a) and Fig. 14(a).

3.4. Higher-order displacement fields

The horizontal displacement and strain field functions are expressed via Eq. (8) through Eq. (10):

$$u(x) = \varepsilon_{\max} x,\ \varepsilon(x) = \varepsilon_{\max} \tag{8}$$

for the case of linear displacement and constant strain,

$$u(x) = \frac{\varepsilon_{\max}}{2L} x^2,\ \varepsilon(x) = \frac{\varepsilon_{\max}}{L} x \tag{9}$$

for the case of quadratic displacement and linear strain, and

$$u(x) = \frac{\varepsilon_{\max}}{3L^2} x^3, \quad \varepsilon(x) = \frac{\varepsilon_{\max}}{L^2} x^2 \tag{10}$$

for the case of cubic displacement and quadratic strain, where L is the length of the low-resolution image in the horizontal (x) direction (400 pixel), and $\varepsilon_{\max}$ is the maximum horizontal strain imposed. For brevity, only numerical simulation results for maximum tensile strains between 250 and 20,000 με are presented. However, it is noted that similar results were attained for compression strain fields with maximum compression strain between -250 and $-20{,}000$ με. These $|\varepsilon_{\max}|$ values cover a relevant range for representative structural materials subjected to service and ultimate stress levels, such as concrete and masonry (ultimate tensile strain $\sim 10^2$ με, ultimate compression strain $\sim 10^3$ με), steel and aluminum (tensile yield strain $\sim 10^3$ με), and fiber reinforced polymer composites (ultimate tensile strain $\sim 10^4$ με).

3.4.1. Linear displacement fields

The horizontal strain imposed is constant (i.e., $\varepsilon_{\max} = \varepsilon$) and the DIC strain measurement uncertainty is uniformly distributed in the horizontal direction. For ε in the range 250–20,000 με, Fig. 15 presents the (mean) RMSE$_\varepsilon$ per Eq. (7) for all 15 × 15 pixel subsets and for each constant strain profile measured for a given σ, plotted as a function of the associated σ. Similar to the case of constant displacement in Fig. 7(b), the uncertainty rapidly decreases as blurring filters are applied, and is minimized σ in the range 0.75–1.25 pixel. The lower bound ($\sigma = 0.75$ pixel) is more effective at smaller strains ($\varepsilon < 1000$ με). For linear displacement fields with strain $\sim 10^2$–10^3 με (up to $\varepsilon = 4000$ με for the data presented), the uncertainty increases for $\sigma > 1.25$ pixel and tends to converge to similar values irrespective of the deformation imposed and level of blurring, as illustrated in Fig. 15(a). Fig. 15(b) shows that for larger strains ($\varepsilon = 20{,}000$ με for the data presented) Gaussian blurring with σ in the range 0.75–1.25 pixel results in a decrease in measurement uncertainty, albeit not as large as for $\varepsilon \sim 10^3$ με, whereas a higher level of blurring marginally increases the uncertainty. This result suggests that the contribution of Gaussian filtering to reducing the uncertainty in the sub-pixel range is predominant compared with that in larger ranges associated with larger deformations, that is, the uncertainty reduction in the sub-pixel range has a smaller impact on the RMSE$_\varepsilon$ values in Fig. 15(b) compared with Fig. 15(a).

3.4.2. Quadratic and cubic displacement fields

For the case of quadratic, cubic and higher-order displacement fields, the uncertainty of horizontal strain measurements using unfiltered images is a function of the imposed strain, and thus varies along the x direction. To facilitate the graphical representation of the uncertainty as a function of the coordinate in the domain $0 \le x \le 400$ pixel, and for displacement fields with different maximum strain, the parameter RMSE$_\varepsilon(x)$ is introduced in Eq. (11):

$$\mathrm{RMSE}_\varepsilon(x) = \sqrt{\frac{\sum_{j=1}^{N_C} (\varepsilon_{\mathrm{DIC},j} - \varepsilon_{\mathrm{IMP},j})^2}{N_C}} \tag{11}$$

where, compared with Eq. (7), the DIC computations are performed only along the vertical (y) direction for $1 \le j \le N_C$ (i.e., considering

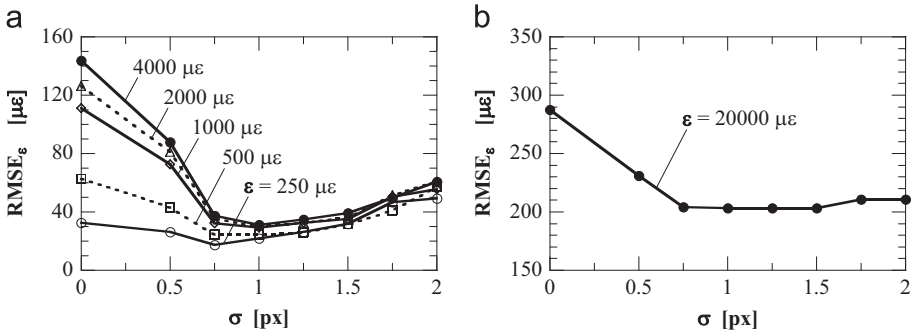

Fig. 15. Relation between measurement uncertainty and Gaussian blurring of down-sampled images for linear displacement and constant strain fields: (a) $RMSE_\varepsilon$ for $250 \le \varepsilon \le 4000$ με, and (b) for $\varepsilon = 20{,}000$ με for $0 \le \sigma \le 2$ pixel.

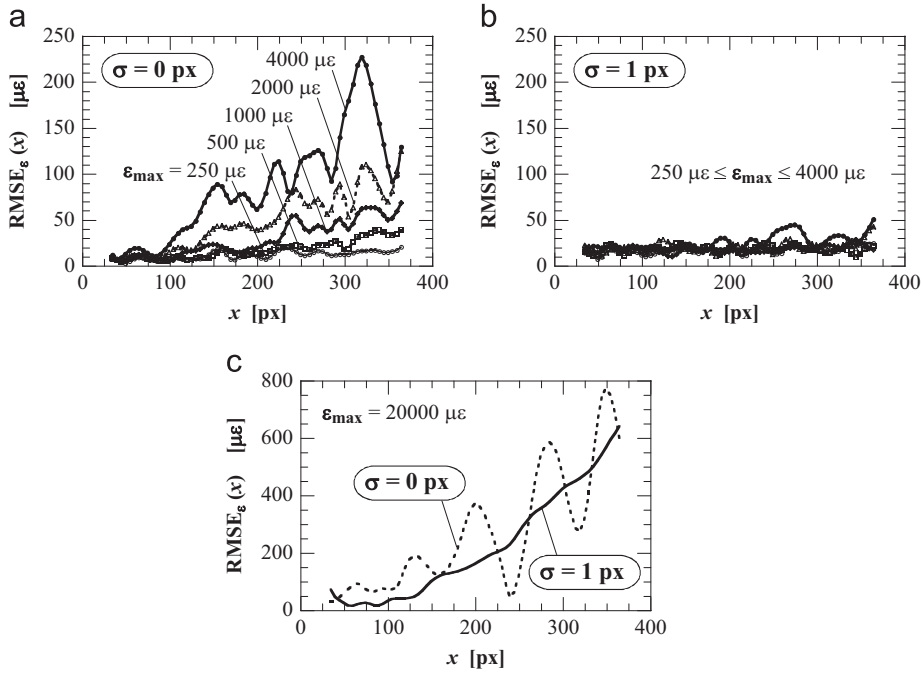

Fig. 16. Relation between measurement uncertainty and Gaussian blurring of down-sampled images for quadratic displacement and linear strain fields: $RMSE_\varepsilon(x)$ for $250 \le \varepsilon_{max} \le 4000$ με from (a) unfiltered and (b) filtered images; and (c) $RMSE_\varepsilon(x)$ for $\varepsilon_{max} = 20{,}000$ με from unfiltered ($\sigma = 0$ pixel) and filtered ($\sigma = 1$ pixel) images.

the columns of the displacement matrix), thus rendering $RMSE_\varepsilon$ as a function of x, which in Eq. (7) is associated with the index i.

For the case of quadratic displacement and linear strain with different ε_{max}, the function $RMSE_\varepsilon(x)$ is presented for a representative unfiltered ($\sigma = 0$ pixel) and filtered ($\sigma = 1$ pixel) set of images in Fig. 16. The outermost 34 pixel portions of the x domain having a length $L = 400$ pixel are neglected to eliminate boundary effects. The uncertainty of DIC measurements using unfiltered images varies with the strain imposed and exhibits an increasing trend as x increases toward more deformed areas, as shown for $250 \le \varepsilon_{max} \le 4000$ με and $\varepsilon_{max} = 20{,}000$ με in Fig. 16(a) and (c), respectively. For linear strain fields with $\varepsilon_{max} \sim 10^2$–$10^3$ με (up to 4000 με for the data presented), Fig. 16(b) shows that image filtering enables to significantly reduce the uncertainty. For example, for $\varepsilon_{max} = 4000$ με, the maximum uncertainty is reduced from 228 με at $x = 319$ pixel to 51 με at $x = 364$ pixel. For linear strain fields with $\varepsilon_{max} \sim 10^4$ με (20,000 με for the data presented), Fig. 16(c) shows that Gaussian filtering becomes less effective in more deformed areas ($x > 150$ pixel). However, filtering enables to essentially eliminate the negative influence of the sub-pixel interpolation bias by reducing the $RMSE_\varepsilon(x)$ function from a sinusoidal shape ($\sigma = 0$ pixel) to a more regular and desirable shape ($\sigma = 1$ pixel). These findings are consistent with those for the case of cubic displacement and quadratic strain fields, as illustrated for $250 \le \varepsilon_{max} \le 4000$ με using an unfiltered ($\sigma = 0$ pixel) and a filtered ($\sigma = 1$ pixel) set of images in Fig. 17(a) and (b), respectively, and for $\varepsilon_{max} = 20{,}000$ με in Fig. 17(c).

4. Interpretation of results

The parametric study presented in Section 3 shows that pre-processing image blurring by means of Gaussian filters with a well-defined range of standard deviations (approximately 0.75–1.25 pixel) results in the overall reduction in DIC measurement errors, irrespective of the degree of the polynomial displacement and strain functions, when using "designer patterns" having well-defined speckles similar to those in Fig. 1(b) and Fig. 3(b) and (c). For strain fields with $\varepsilon_{max} \sim 10^3$ με, a significant decrease in uncertainty is attained as deformations increase. This finding is of practical significance since such levels for ε_{max} are associated with critical deformations under service or ultimate stresses for numerous structural materials. For larger maximum strains ($\varepsilon_{max} \sim 10^4$ με), the reduction in uncertainty is essentially limited to that

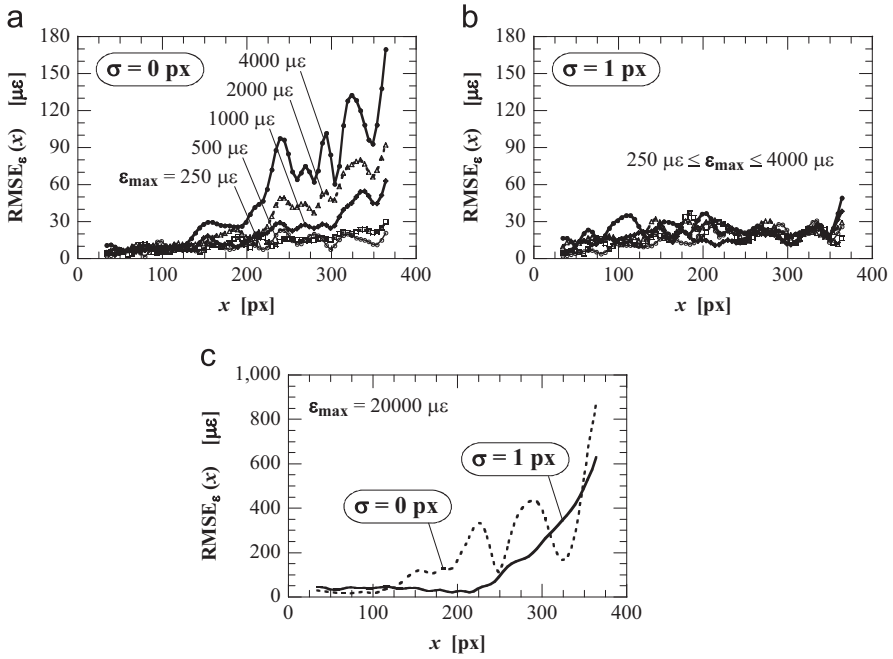

Fig. 17. Relation between measurement uncertainty and Gaussian blurring of down-sampled images for cubic displacement and quadratic strain fields: $RMSE_\varepsilon(x)$ for $250 \le \varepsilon_{max} \le 4000$ με from (a) unfiltered and (b) filtered images; and (c) $RMSE_\varepsilon(x)$ for ε_{max}=20,000 με from unfiltered (σ=0 pixel) and filtered (σ=1 pixel) images.

attributed to the sub-pixel interpolation bias, which notably affects DIC measurements. This finding again is of practical significance since at such level of ε_{max} accurate local measure-ments can hardly be obtained with more conventional means. such as strain gauges and extensometers.

The fact that the range of standard deviations where Gaussian filtering is most effective is largely independent of the displacement and strain functions suggests that this range is primarily dependent on the DIC algorithms. In particular, for a given range of subset sizes, the bias component of the displacement estimation error is strongly related to the intensity interpolation method as long as the subset size is chosen sufficiently large to provide a nominally isotropic and homogeneous random pattern [25]. In fact, unfiltered images are characterized by steep transients between dark speckles and light background with associated high-frequency content in the image spectra (Fig. 4), which cannot be closely represented by the polynomial interpolation of the intensity pattern that follows the subset deformation according to a given shape function. When these contributions are not filtered, they produce an aliasing effect on the subset interpolation. Filtering becomes effective when the spectral portion having a higher frequency content than that of the interpolation function is minimized, whereas more blurring may result in the loss of frequency content that can be effectively described by the interpolation function, thereby increasing the measurement uncertainty.

The comparison of the auto-correlation functions of the brightness profile for a representative unfiltered (σ=0 pixel) and filtered (σ=1 pixel) high-resolution image, which are plotted in Fig. 18, provides a mathematical explanation of why the high-frequency information contained in the brightness profile of the speckle pattern in Fig. 3(b) and (c) cannot be accurately approximated by the polynomial interpolation function used in the DIC analysis, unless Gaussian blobs are used in lieu of speckles with well-defined edges. In fact, in the case of the unfiltered image, the discontinuity of the auto-correlation function at the origin (shift=0 pixel) indicates that the image is characterized by a non-differentiable brightness profile, thus preventing an efficient approximation via polynomial interpolation. Conversely, the

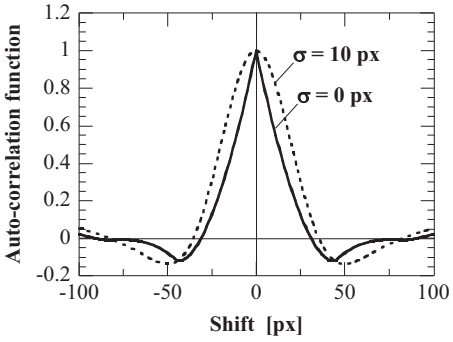

Fig. 18. Auto-correlation function of unfiltered (σ=0 pixel) and filtered (σ=10 pixel) high-resolution image with speckle pattern in Fig. 3(b). Note that σ=10 pixel is equivalent to σ=1 pixel for × 10 down-sampled image.

brightness profile of the filtered image is differentiable as indicated by the parabolic maximum at the origin, thus facilitating an efficient polynomial approximation. It is concluded that an appropriate interpolation procedure for subset matching can be devised, provided that the images are moderately blurred when using a high-contrast speckle pattern with well-defined speckles and size (resulting in relatively high-frequency components as shown in Fig. 4). Commonly used spray-painted speckle patterns are more suitable for polynomial interpolation [9]. Here, moderate image blurring does not alter the near-zero frequency peak nor narrow the non-zero frequency range (Fig. 13), while tending to minimize sinusoidal bias error trends [9,14] and modestly reduce DIC measurement uncertainty (Fig. 14).

In regard to the influence of Gaussian filtering on the random component of the estimated displacement error, two opposite effects are concurrently present, namely: (1) a decrease in intensity pattern noise, which results in a reduction of the numerator of Eq. (2), with a beneficial effect in reducing uncertainty; and (2) a decrease in the brightness matrix gradients, which results in a reduction of the denominator of Eq. (2), thus contributing to increasing the uncertainty. The combined effect is a reduction of the random component of the error for "designer patterns",

whereas for typical spray-painted speckle patterns Gaussian blurring is only beneficial in reducing bias errors.

5. Stability of effect of image filter pre-processing

Following the methodology in Fig. 2(a) used for the numerical study presented, numerical simulations are performed for the representative case of linear displacement and constant strain (1000, 4000 and 20,000 με) fields. Here, the effects of image intensity pattern noise (which is always present in actual measurements), subset size, and frequency content are evaluated. The strain measurement uncertainty is quantified by means of $RMSE_\varepsilon$ in Eq. (7) accounting for all 15 × 15 pixel subsets for each constant strain profile measured for a given σ, similar to Fig. 15.

5.1. Influence of image noise

In all imaging systems, a random amount of uncorrelated noise is present in the camera output analog signal for a given pixel. The influence of noise can be minimized by averaging multiple images, which must be taken while no additional deformations are imposed. Random noise is simulated by means of the percent additive noise [7], Γ, defined in Eq. (12):

$$\Gamma = \frac{s}{\Delta I} 100\% \tag{12}$$

For a predefined value of Γ, s is the standard deviation of a normal distribution from which a random amount is extracted and added to each pixel, and ΔI is the image intensity pixel range (equal to 225-30 for this study). The simulated Γ ranges from 0% (no noise) to 5%, where 0.5% is a reasonable value for a typical camera. Representative $RMSE_\varepsilon$ values are plotted for different noise levels as a function of the Gaussian standard deviation for a constant strain ε of 1000, 4000 and 20,000 με in Fig. 19(a)–(c), respectively. At relatively low noise levels (Γ=0.5–1%) the range of σ at which uncertainty is minimized is not affected. At relatively high noise levels (Γ=5%) the influence of noise is predominant and Gaussian blurring becomes ineffective.

5.2. Influence of subset size

The low-resolution images from the constant strain simulation are analyzed with different subset sizes: 9 × 9, 15 × 15, 33 × 33 and 63 × 63 pixel, which is reasonably considered a large subset [26]. The overlap is set to one third of the subset size. It is noted that by changing the subset size, its influence on the effect of image

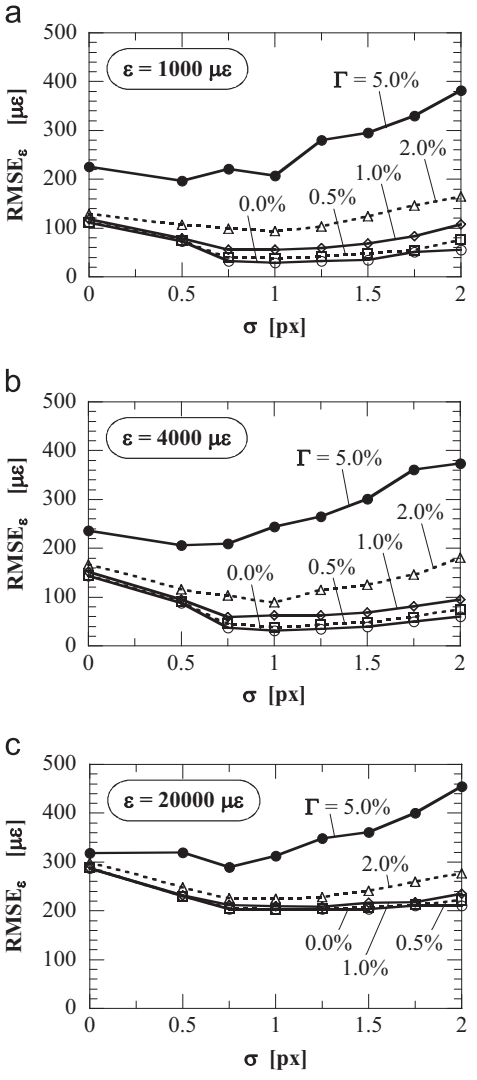

Fig. 19. Influence of image noise for constant strain fields: $RMSE_\varepsilon$ as function of σ for (a) ε=1000, (b) 4000, and (c) 20,000 με for $0 \le \Gamma \le 5\%$ for $0 \le \sigma \le 2$ pixel.

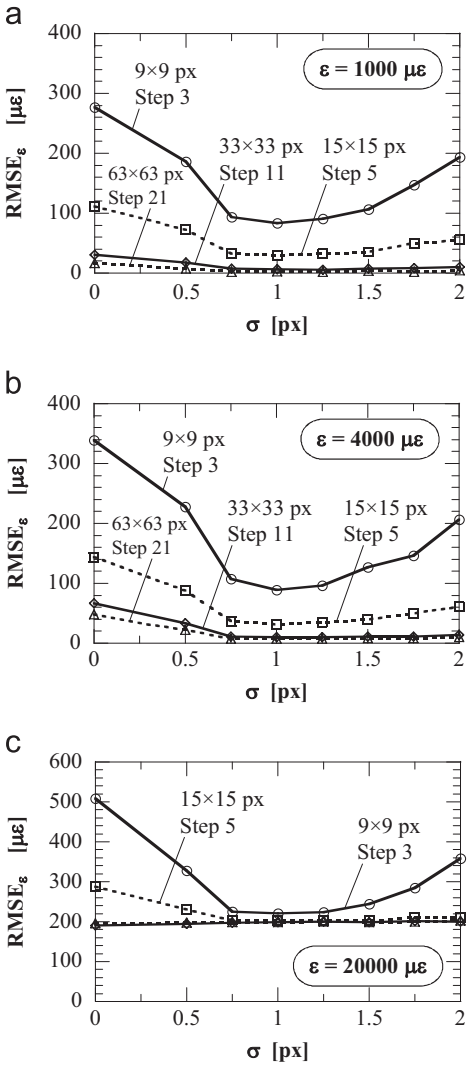

Fig. 20. Influence of subset size for constant strain fields: $RMSE_\varepsilon$ as function of σ for (a) ε=1000, (b) 4000, and (c) 20,000 με for 9 × 9, 15 × 15, 33 × 33 and 63 × 63 pixel subset size.

blurring is inevitably assessed at varying spatial resolutions of the DIC measurements.

Representative $RMSE_\varepsilon$ values are plotted for different subset sizes as a function of σ, for a constant strain ε of 1000, 4000 and 20,000 με, in Fig. 20(a)–(c), respectively. Results show that subset size does not affect the range of standard deviations at which uncertainty is minimized. The sensitivity to relatively large levels of blurring decreases with increasing subset size. However, an increase in subset size negatively affects spatial resolution, prompting the need to compromise between uncertainty and resolution when designing a DIC setup. It is also noted that as the strain increases the images are more affected by digital (resampling and quantization) noise introduced through the strain computation procedure. As a result, the effect of image blurring is muted under larger strains, as confirmed in Fig. 20(c) for $\varepsilon_{max}=20{,}000$ με.

5.3. Influence of frequency content of speckle pattern

Constant strain fields and DIC measurements are simulated on low-resolution images for each of the four speckle patterns in Fig. 21. Different frequency contents are rendered by varying the speckle diameter, D (between 2 and 8 pixel), and the average on-center spacing between adjacent speckles, d (between 3 and 12 pixel). It is noted that the case $D=2$ pixel corresponds to a minimally sampled speckle where errors are generally expected to be higher. All remaining cases have $D>4$ pixel, which is an appropriately oversampled condition [6,9]. Representative $RMSE_\varepsilon$ values are plotted for different values of speckle size, D, and spacing, d, as a function of σ, for a constant strain ε of 1000, 4000 and 20,000 με in Fig. 22(a)–(c), respectively. When using unfiltered images ($\sigma=0$ pixel), smaller speckles and distances ($D=2$ pixel, $d=3$ pixel) allow to better reduce the uncertainty. However, Gaussian filtering results in better uncertainty reduction for larger speckle sizes and distances, with no significant increase for stronger Gaussian blurs. The range of standard deviations at which uncertainty is minimized does not change irrespective of the frequency content. In fact, effective blurring affects the areas of steep transition between speckles (of any size and spacing) and background, which are associated with high-frequency components and provide a negligible contribution to the low-frequency content.

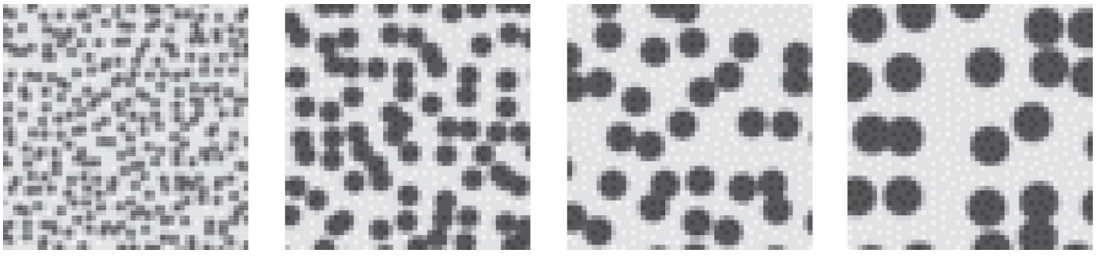

Fig. 21. Numerically simulated speckle patterns: 50 × 50 pixel samples with D=speckle diameter, and d=average speckle on-center spacing.

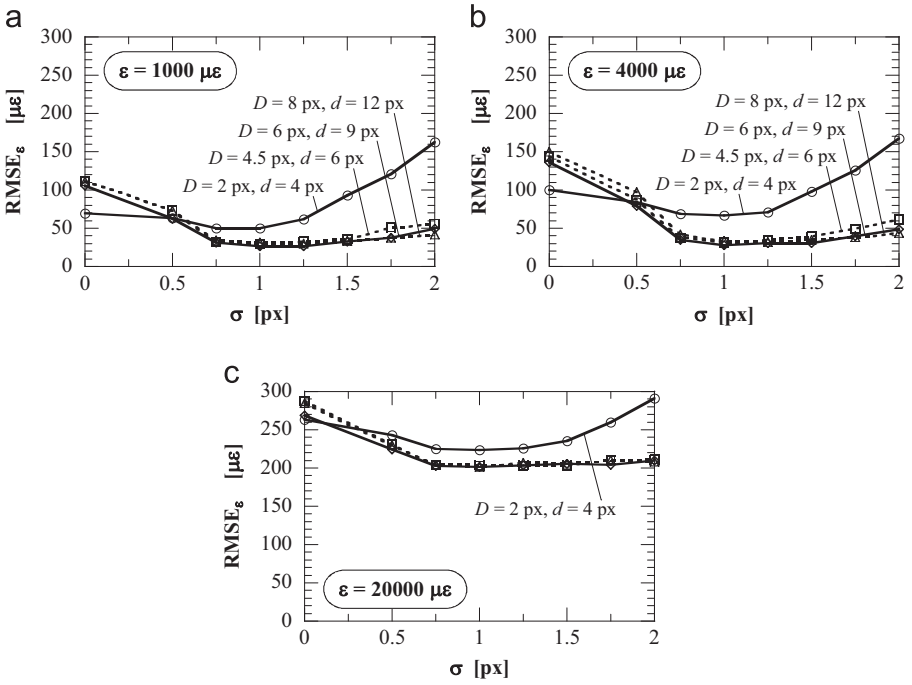

Fig. 22. Influence of frequency content of speckle pattern for constant strain fields: $RMSE_\varepsilon$ as function of σ for (a) $\varepsilon=1000$, (b) 4000, and (c) 20,000 με for simulated speckle patterns

6. Conclusions

The first part of this paper presents a numerical and experimental study of the effect of Gaussian pre-filtering on the uncertainty of DIC measurements for the specific case of high-contrast "designer patterns" having speckles with well-defined and consistent shape, size and spacing. These patterns can be numerically designed and applied on the measurement surface using printed coatings or pre-cut stencils, and are ideal when using standard-resolution cameras to acquire images of large regions of interest on full-scale specimens (e.g., concrete and masonry walls). The following conclusions are drawn.

1. Pre-processing image blurring using Gaussian filters with a well-defined range of standard deviations (0.75–1.25 pixel) results in the minimization of bias error as well as uncertainty in DIC measurements irrespective of the degree of the polynomial functions describing displacement and strain fields.
2. The effectiveness of a given Gaussian standard deviation depends primarily on the DIC algorithm. Uncertainty is minimized by using blurred images resulting from the filtering of high-frequency components, increasing the accuracy of the interpolation process.
3. For constant displacement (zero strain) fields, a decrease in uncertainty is attained in the sub-pixel range where it is more of concern.
4. For strain fields with maximum tensile or compressive strain of $\sim 10^2$–10^3 $\mu\varepsilon$, a significant decrease in uncertainty is attained as deformations increase. This finding is of practical significance as such maximum strain levels are associated with critical deformations under service and ultimate stress levels for most structural materials (ranging from brittle ceramics to ductile metals).
5. For strain fields with maximum tensile or compressive strain of $\sim 10^4$ $\mu\varepsilon$, the decrease in uncertainty is essentially limited to that attributed to the sub-pixel interpolation bias. This finding is of practical significance as at such maximum strain levels accurate local measurements can hardly be obtained with conventional point-wise sensors (e.g., strain gauges and extensometers).

Conversely, for typical spray-painted speckle patterns without well-defined particle shape, size and spacing, image blurring is only beneficial in reducing bias errors [9,14]. In the second part of the paper, the stability of the effect of Gaussian pre-filtering on a "designer pattern" is tested through simulations for the case of linear displacements at varying maximum strains, using different levels of image noise (which is always present in real-case applications), subset size, and speckle pattern frequency content. It is concluded that the range of Gaussian standard deviations for which uncertainty is minimized does not change except for extreme (and most likely unrealistic) noise levels. In particular, if a Gaussian blur with a standard deviation of 0.75 pixel is used, then all over-sampled speckle patterns yield essentially the same result.

Acknowledgements

The collaborative research presented herein was made possible through the financial and logistic support of the University of South Carolina and the Politecnico di Milano, and partial funding from the US National Science Foundation under grant no. CMMI-1049483. These sources of support are gratefully acknowledged. Special thanks are extended to Correlated Solutions, Inc. (Columbia, SC) for providing the software Vic-2D free of charge.

References

[1] Bruck HA, McNeil SR, Sutton MA, Peters III WH. Digital image correlation using Newton–Raphson method of partial differential correction. Exp Mech 1989;29:261–7.
[2] Pan B, Qian K, Xie H, Asundi A. Two-dimensional digital image correlation for in-plane displacement and strain measurement: a review. Meas Sci Technol 2009;20:062001 (17 pp).
[3] Zhou P, Goodson KE. Subpixel displacement and deformation gradient measurement using digital image/speckle correlation (DISC). Opt Eng 2001;40:1613–20.
[4] Lecompte D, Smits A, Bossuyt S, Sol H, Vantomme J, Van Hemelrijck D, et al. Quality assessment of speckle patterns for digital image correlation. Opt Lasers Eng 2006;44:1132–45.
[5] Pan B, Xie H, Wang Z, Qian K, Wang Z. Study on subset size selection in digital image correlation for speckle patterns. Opt Express 2008;16:7037–48.
[6] Sutton MA, Orteu J-J, Schreier HW. Image correlation for shape, motion and deformation measurements. New York, NY: Springer; 2009.
[7] Wang YQ, Sutton MA, Bruck HA, Schreier HW. Quantitative error assessment in pattern matching: effects of intensity pattern noise, interpolation, strain and image contrast on motion measurements. Strain 2009;45:160–78.
[8] Pan B, Lu Z, Xie H. Mean intensity gradient: an effective global parameter for quality assessment of the speckle patterns used in digital image correlation. Opt Lasers Eng 2010;48:469–77.
[9] Schreier HW, Braasch JR, Sutton MA. Systematic errors in digital image correlation caused by intensity interpolation. Opt Eng 2000;39:2915–21.
[10] Berg AC, Malik, J. Geometric blur for template matching. In: Proceedings of 2001 IEEE computer society conference on computer vision and pattern recognition (CVPR 2001):I-607–I-614, 2001.
[11] Cantatore A, Cigada A, Sala R, Zappa E. Hyperbolic tangent algorithm for periodic effect cancellation in sub-pixel resolution edge displacement measurement. Measurement 2009;42:1226–32.
[12] El-Hajjar RF, Petersen DR. Adhesive polyvinyl chloride coatings for quantitative strain measurement in composite materials. Composites Part B 2011;42:1929–36.
[13] Ghorbani R, Matta F, Sutton MA. Full-Field deformation measurement and crack mapping on confined masonry walls using digital image correlation. Exp Mech 2014:17. http://dx.doi.org/10.1007/s11340-014-9906-y.
[14] Pan B. Bias error reduction of digital image correlation using Gaussian pre-filtering. Opt Lasers Eng 2013;51:1161–7.
[15] International Organization for Standardization. ISO 16610-21:2011 Geometrical product specifications (GPS) – Filtration – Part 21: Linear profile filters: Gaussian filters. Geneva, Switzerland: ISO; 2011.
[16] Society for Experimental Mechanics Digital Image Correlation Challenge. High contrast subpixel sample images, ⟨http://www.sem.org/images/dic-challenge/HighContrastImages.zip⟩ [accessed April 4, 2014].
[17] Reu PL. Experimental and numerical methods for exact subpixel shifting. Exp Mech 2011;51:443–52.
[18] Zappa E, Mazzoleni P, Matinmanesh A. Uncertainty assessment of digital image correlation method in dynamic applications. Opt Lasers Eng 2014;56:140–51.
[19] Lecompte D, Sol H, Vantomme J, Habraken A. Analysis of speckle patterns for deformation measurements by digital image correlation. Proc SPIE 200663410E.
[20] Bornert M, Brémand F, Doumalin P, Dupré J-C, Fazzini M, Grédiac M, et al. Assessment of digital image correlation measurement errors: methodology and results. Exp Mech 2009;49:353–70.
[21] Aubury M, Luk W. Binomial filters. J VLSI Sig Proc 1996;12:35–50.
[22] International Organization for Standardization. ISO/IEC Guide 98-3:2008 Uncertainty of measurement—Part 3: guide to the expression of uncertainty in measurement (GUM:1995). Geneva, Switzerland: ISO; 2008.
[23] Cheli F, Mazzoleni P, Pezzola M, Ruspini E, Zappa E. Vision-based measuring system for rider's pose estimation during motorcycle riding. Mech Syst Sig Process 2013;38:399–410.
[24] Lee S-Y, Kumar Y, Cho J-M, Lee S-W, Kim S-W. Enhanced autofocus algorithm using robust focus measure and fuzzy reasoning. IEEE Trans Circuits Syst Video Technol 2008;18:1237–46.
[25] Schreier HW, Sutton MA. Systematic errors in digital image correlation due to undermatched subset shape functions. Exp Mech 2002;42:303–10.
[26] Yaofeng S, Pang JHL. Study of optimal subset size in digital image correlation of speckle pattern images. Opt Lasers Eng 2007;45:967–74.